Article

Microanalytical Mass Spectrometry with Super-Resolution Microscopy Reveals a Proteome Transition During Development of the Brain's Circadian Pacemaker

Sam B. Choi,[#] Tarlan Vatan,[#] Theresa A. Alexander,[#] Chenghang Zhang, Shyrice M. Mitchell, Colenso M. Speer,* and Peter Nemes*

Read Online

ACCESS | 📊 Metrics & More | 📰 Article Recommendations | 🆂🇮 Supporting Information

ABSTRACT: During brain development, neuronal proteomes are regulated in part by changes in spontaneous and sensory-driven activity in immature neural circuits. A longstanding model for studying activity-dependent circuit refinement is the developing mouse visual system where the formation of axonal projections from the eyes to the brain is influenced by spontaneous retinal activity prior to the onset of vision and by visual experience after eye-opening. The precise proteomic changes in retinorecipient targets that occur during this developmental transition are unknown. Here, we developed a microanalytical proteomics pipeline using capillary electrophoresis (CE) electrospray ionization (ESI) mass spectrometry (MS) in the discovery setting to quantify developmental changes in the chief circadian pacemaker, the suprachiasmatic nucleus (SCN), before and after the onset of photoreceptor-dependent visual function. Nesting CE-ESI with trapped ion mobility spectrometry time-of-flight (TOF) mass spectrometry (TimsTOF PRO) doubled the number of identified and quantified proteins compared to the TOF-only control on the same analytical platform. From 10 ng of peptide input, corresponding to <∼0.5% of the total local tissue proteome, technical triplicate analyses identified 1894 proteins and quantified 1066 proteins, including many with important canonical functions in axon guidance, synapse function, glial cell maturation, and extracellular matrix refinement. Label-free quantification revealed differential regulation for 166 proteins over development, with enrichment of axon guidance-associated proteins prior to eye-opening and synapse-associated protein enrichment after eye-opening. Super-resolution imaging of select proteins using STochastic Optical Reconstruction Microscopy (STORM) corroborated the MS results and showed that increased presynaptic protein abundance pre/post eye-opening in the SCN reflects a developmental increase in synapse number, but not presynaptic size or extrasynaptic protein expression. This work marks the first development and systematic application of TimsTOF PRO for CE-ESI-based microproteomics and the first integration of microanalytical CE-ESI TimsTOF PRO with volumetric super-resolution STORM imaging to expand the repertoire of technologies supporting analytical neuroscience.
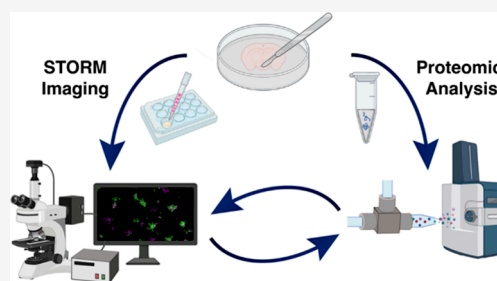
INTRODUCTION

Light is an essential signal for synchronizing the body's internal clock with the diurnal cycle, and irregular patterns of light exposure can result in sleep disruption, mood disorders, and depression.[1,2] Circadian entrainment to light is regulated by intrinsically photosensitive retinal ganglion cells (ipRGCs) in the retinae, which relay luminance information to the brain's circadian pacemaker, the suprachiasmatic nucleus (SCN).[1,3] In the mature brain, signaling from ipRGCs to the SCN drives changes in gene expression and protein production that are essential for circadian physiology.[4] Previous mass spectrometry (MS)-based studies were instrumental in characterizing the rodent SCN proteome including identification of neuropeptide expression and release[5,6] as well as measurement of circadian and light-induced changes in protein expression.[7−11] However, little is known about developmental changes in the SCN proteome, a limited tissue microenvironment, such as those that may be driven by changes in sensory input pre/post eye-

opening. Development of analytical technologies with improved sensitivity, molecular specificity, and spatiotemporal scalability would help characterization of proteomes from the developing SCN and other small brain nuclei.

Only recently has MS technology been advanced to sufficient sensitivity to characterize limited-to-trace amounts of proteomes. From milligrams to micrograms of starting proteome amounts, conventional nanoflow high-performance liquid chromatography (HPLC) MS is able to detect deep proteomes, including over 13,000 proteins by analyzing typically ∼100 ng to
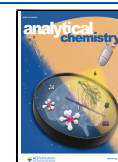
~1 μg of protein content per measurement.[12,13] Specialized approaches were introduced to extend HPLC-MS to nanograms of proteomes or less. For example, the data-dependent acquisition (DDA) method identified up to 1400 proteins[14] whereas data-independent acquisition returned up to ~1600 proteins[15] from single cells in *Xenopus laevis* embryos using HPLC-MS. NanoPOTS (N-2) arrays were used on 100 pg of protein digest to identify ~1300 proteins from single murine cells and ~1000 proteins from an ~100-μm section of the brain containing ~10−18 cells.[16] The automated single-cell proteomics workflow (ScoPE2) on 200 single cells reported an average of ~1000 proteins per cell.[17] Recently, trapped ion mobility spectrometry time-of-flight (TimsTOF) MS was developed to enable the detection of 2500 proteins from ~10 ng of HeLa proteome[18] and 843 proteins from up to 430 single HeLa cells.[19]

Capillary electrophoresis (CE) MS has emerged as an alternative technology to explore proteomes in microenvironments, small populations of cells, and single cells. CE is adaptable to trace amounts of samples, identifying ~300−1000 proteins from ~100 pg[20,21] to 1 pg[22] of proteomes. Custom-built CE-MS platforms allowed for identifying ~800 different proteins from ~5 ng of protein aspirates from single cells in *X. laevis*,[23,24] 428 different proteins from ~5 ng (~100 neurons) in the mouse brain,[25] and ~100 proteins from 16 pg of the *Escherichia coli* proteome.[26] Most recently, we have introduced patch-clamp proteomics using CE-MS, which allowed for ~150 proteins to be identified from ~1 pg of protein digest from the soma of an electrophysiologically characterized dopaminergic neuron in the mouse substantia nigra.[22] Commercial CE instruments equipped with high-sensitivity CE-ESI ion sources were employed to detect 1249 proteins from ~300 ng of *X. laevis* egg proteome,[27] 744 proteins from single HeLa-cell-equivalent protein digests,[28] and 1000 proteins from 880 pg and 160 proteins from ~88 pg of HeLa protein digest standard.[28] With further improvements in sensitivity, microanalytical CE-MS has important future potential for interrogating the molecular composition of brain regions and neuronal cell types.

Here, our goal was to improve microanalytical proteomics for characterizing the translational state of the limited SCN proteome. Our analytical objectives were (1) to enhance sensitivity in custom-built microanalytical CE-ESI-MS to enable deep proteomics in the tissue and (2) to leverage this information on gene translation to guide super-resolution imaging of developmentally regulated synaptic proteins critical for circuit function. This study was focused on the mouse SCN at two important time points of visual system development, before (postnatal day, P, 8) and after (P21) the onset of rod/cone-dependent visual function. Following recent developments in LC TimsTOF PASEF MS,[18] we proposed that supplementing microanalytical CE-ESI with ion trapping and a second-dimension ion-mobility separation via TimsTOF PRO MS would deepen the detectable portion of the SCN proteome, improve utilization of the tandem MS duty cycle, and reduce spectral interferences. After systematically assessing the analytical metrics of performance, we aimed to quantify changes in the local tissue proteome before and after eye-opening. To further contextualize the results revealed by CE-MS, we measured the spatial organization of targeted proteins using multicolor volumetric super-resolution STochastic Optical Reconstruction Microscopy (STORM). The results from microanalytical CE-ESI-MS-guided STORM provided previously unavailable information about developmental changes in critical presynaptic proteins with important implications for SCN circuit maturation.

EXPERIMENTAL PROCEDURES

Materials, Animals, and Procedures. A detailed account of materials, animals, tissue collection and processing, proteomics, STORM imaging, and data analysis is provided in the electronic Supporting Information (SI) document. All animal work was performed in accordance with a protocol approved by the Institutional Animal Care and Use Committee at the University of Maryland, College Park (approval no. R-JUL-20-39).

Experimental Design. To account for biological variability, four to five different SCNs were collected for the final study, each from a different mouse (biological replicates, BR). Each BR was analyzed in three technical replicates (TRs: same sample measured repeatedly) using CE-ESI-TimsTOF PRO MS. Tissues from both sexes were analyzed in this project.

Safety Considerations. Capillaries, which pose a needle-stick hazard, were handled with attention. Common safety protocols were followed for the handling of chemicals. All electrically conductive parts of the CE-ESI interface were shielded (earth-grounded or isolated) to prevent electrical shock hazard.
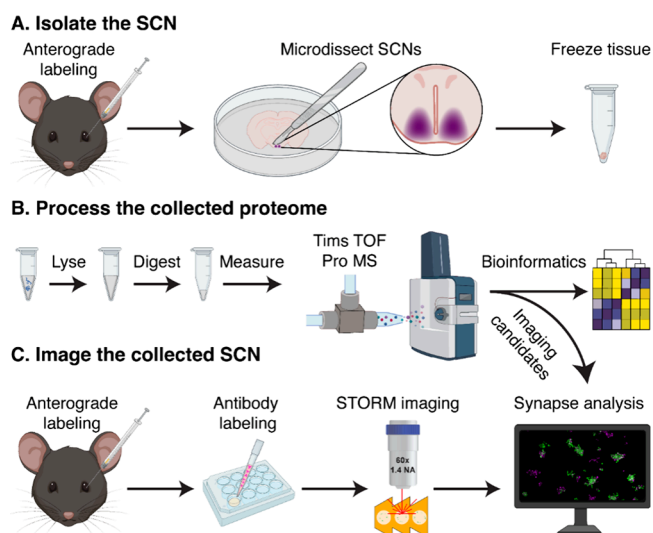

Figure 1. Overview of the experimental workflow integrating microanalytical MS proteomics and super-resolution optical imaging to assess spatiotemporal proteome changes in the developing SCN. (A) Projections from the retinae to the SCN were labeled at postnatal day (P) 7 and P20 by intravitreal injection with CTβ-488 and, 1 day later, the SCN tissues were microdissected and flash-frozen in liquid nitrogen. (B) The proteome was extracted from the collected tissues, processed, and profiled on a custom-built CE-ESI platform using TimsTOF PRO PASEF MS. (C) The results were corroborated using single-molecule localization super-resolution imaging. Samples were prepared by anterograde tracing at P7 and P20, followed by tissue collection at P8 and P21, immunolabeling, and imaging with STORM.

Data Availability. The MS proteomics data were deposited to the ProteomeXchange Consortium via the PRIDE[29] partner repository with the data set identifier PXD038245. All codes used for bioinformatic analyses including principal component analysis, differential expression, and heatmap clustering can be found in the GitHub repository: https://github.com/SpeerLab/SCN_proteomics.

RESULTS AND DISCUSSION

Discovery Microproteomics of the SCN. We sought to profile the developing SCN proteome at two important time points, before and after eye-opening (Figure 1). We performed anterograde tract tracing by cholera toxin ß subunit (CTß) injections to visualize and microdissect ~0.1−0.3 mm³ of SCN tissue from individual brain sections (Figure 1A). Although this tissue contained sufficient proteome amounts for LC-MS analysis (~2−5 μg proteome based on a total protein assay), we chose to test the scalability of CE-ESI-MS for tissue microproteomics. A total of ~10 ng of proteome digest was measured, which approximates to ~40 cells (Table 1). After

Table 1. Assessment of Scalability for Microanalytical Proteomics Using CE-ESI-TimsTOF PRO MS.[a]

measured SCN proteome	estimates to	identified proteins
10 ng	40 cells	1572
1 ng	4 cells	736
500 pg	2 cells	659
100 pg	subcellular	365

[a]Cumulative number of protein identification is reported based on three technical triplicate analyses.

configuring CE-ESI TimsTOF PRO PASEF for sensitivity (Figure 1B), we quantified the proteome composition in the SCN over development. Using differential expression (DE) analyses, we identified key synaptic and cellular proteins with differential regulation after eye-opening, thus providing candidates for future studies assessing biological significance. Last, we investigated the spatial organization and relative abundance of developmentally upregulated synaptic proteins using super-resolution imaging via volumetric STORM (Figure 1C).

Initially, to deepen the detectable proteome, we enhanced the sensitivity of CE-ESI-MS by complementing solution-phase separation with gas-phase separation via ion mobility spectrometry (IMS). We reasoned that TimsTOF PRO would provide several advantages for CE-ESI-MS proteomics. First, the time frame of IMS (~100 ms/spectrum) naturally nests within the typical peak widths peptides have during electrophoretic separation (5−15 s temporal peaks in our data). Similar to its integration with LC-MS, we expected IMS to expand the net peak capacity of the system to improve bandwidth utilization during DDA. Furthermore, ion accumulation by trapped IMS (TIMS) promised enhanced detection sensitivity. Although PASEF MS has been developed and well-tested on LC-ESI instruments, the approach has not yet been systematically evaluated for CE-MS, where the mechanisms of separation are different.

We systematically increased the sensitivity of CE-ESI and TimsTOF PRO (Figure 2A). The frequency of the PASEF cycle, target ion intensity, and collision energy for peptide sequencing were each sequentially adjusted to maximize proteome coverage (Figure 2A). To facilitate technology optimization and characterization, we eliminated biological variability from this portion of the study by pooling SCN tissues from nine mice to
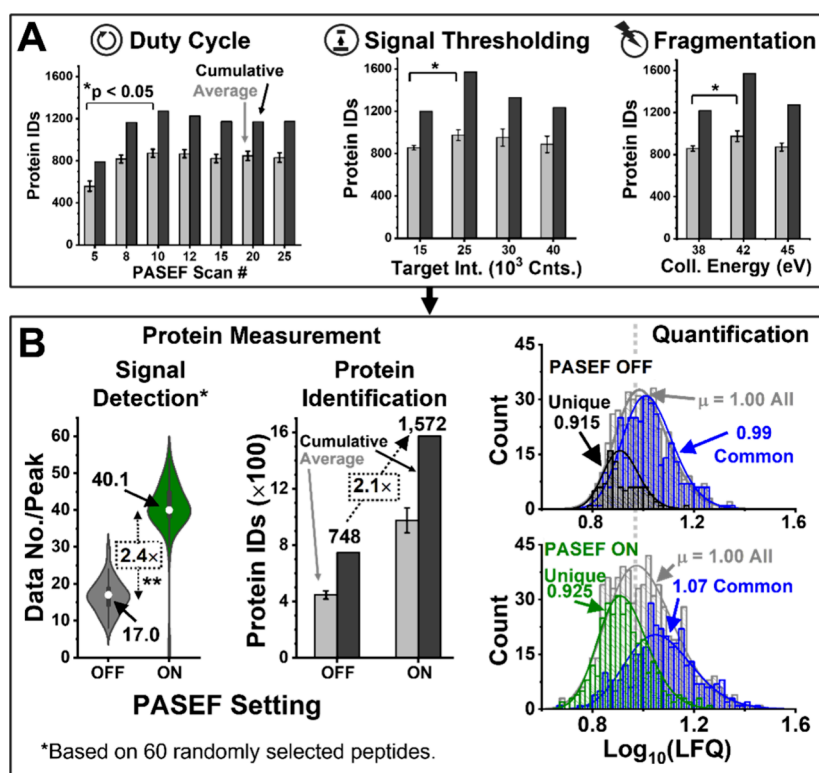

Figure 2. System configuration for sensitive SCN proteomics. (A) Optimization in duty cycle of PASEF transitions (scans) as well as the signal thresholding and energy of peptide fragmentation for sequencing (in this order). (B) (Left panel) A higher duty cycle allowed PASEF MS to more than double the rate of data sampling, as shown for 60 randomly selected peptides. (Middle panel) Engagement of PASEF more than doubled identifications on the TOF-MS system, finding 1572 different proteins from ~10 ng, or <0.5% of the total extracted SCN proteome. (Right panel) The calculated LFQ values revealed the TimsTOF PRO PASEF-identifiable proteins at the lower domain of the quantified linear concentration range. In all panels, key to statistics (*$p < 0.05$ and **$p < 0.005$, Student's t test) and colors (cumulative results, dark gray; average results, gray).
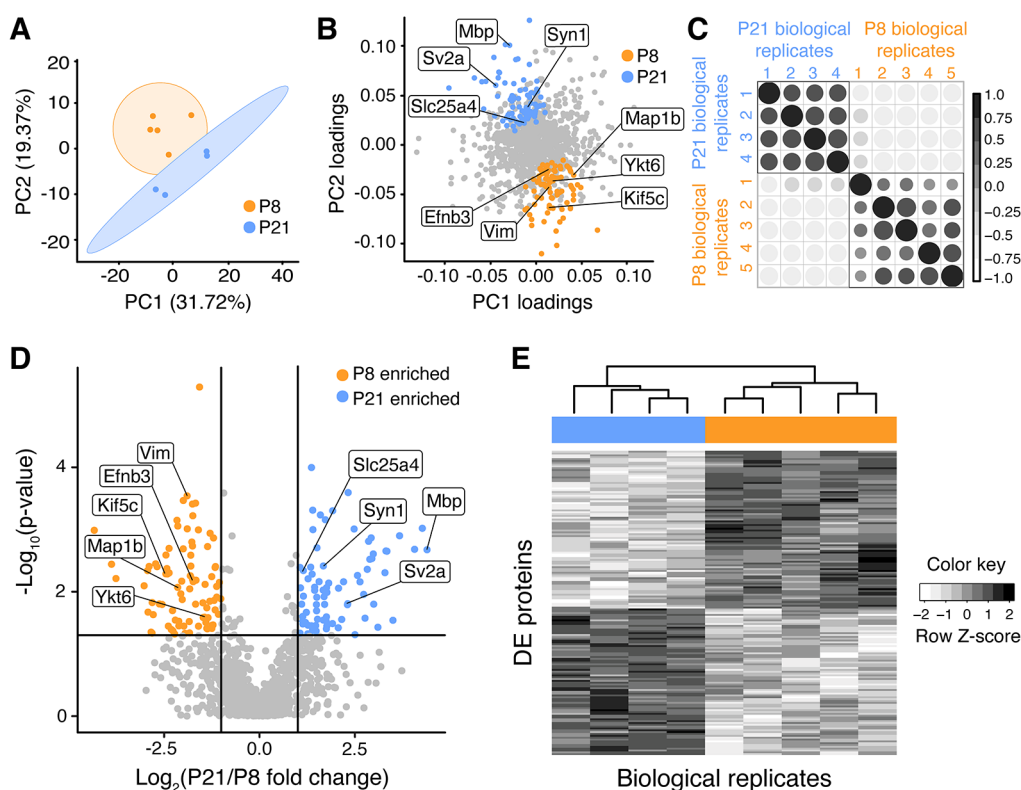
Figure 3. Quantitative comparison of the SCN proteome before and after eye-opening based on the CE-ESI TimsTOF PRO MS identification of 1894 proteins. (A) Score plot from unsupervised PCA on 1066 proteins quantified reveals age-dependent clustering of global proteomic differences with 95% confidence intervals (ovals). (B) Loading plot shows proteins with the largest contribution to the observed differences. Color-coding marks developmental time-points. (C) A correlation matrix analysis reveals significant associations within, but not between, biological replicates at each developmental age. Pearson correlation coefficients are color coded from complete positive correlation (black) to anticorrelation (white). (D) Volcano plot shows 166 proteins with significant differential expression between the developmental time points. Fold change cutoff = 2. Adjusted p value cutoff = 0.05. (E) Heat map for the 166 differentially expressed proteins before and after eye-opening reveals two distinct clusters. Blue/gold = P21 and P8 biological replicates, respectively. Color key: white reflects relative protein depletion, and black reflects relative protein enrichment.

prepare a stock proteome digest for analyses. Measurement of 10 ng of the resulting proteome returned ∼748 proteins in technical triplicate using TOF-only detection (without TIMS). With each dissected SCN tissue yielding ∼2−5 μg of proteome on average based on a total protein assay, these analyzed sample amounts correspond to less than ∼0.5% of the SCN proteome. Analysis of a higher amount of the proteome is, of course, anticipated to yield sensitivity enhancements and is feasible using large-volume sample stacking CE[30] or LC-MS. By deliberately under-sampling the available SCN proteome in this study, we aimed to establish proof-of-concept scalability to limited populations of neurons (∼40 cells, Table 1).

CE-ESI TimsTOF PRO was benchmarked against TOF-MS, the closest neighboring technology for reference; the PASEF operational modality was engaged or disengaged on the same mass spectrometer during these experiments. From 10 ng of SCN proteome, the TimsTOF method returned ∼1572 different proteins between technical triplicate pilot analyses (data not shown). Figure 2B evaluates the quantitative performance between the approaches. We randomly selected 60 proteotypic peptides that were present at low, middle, and high concentrations based on calculated label-free quantification (LFQ) indices.[31] PASEF increased the sampling rate from an average of ∼17 to ∼40 data points per electropherographic peak (left panel), marking a statistically significant increase in data acquisition rate ($p = 4.48 \times 10^{-30}$, Student's t test). Faster sequencing in turn allowed PASEF to more than double the

number of identifiable proteins compared to DDA TOF (middle panel). The limits of quantification were benchmarked in terms of the dynamic range and relative concentration of the proteins that were quantified based on LFQ. The computed LFQ concentration values were $\log_{10}$-transformed and mean-center normalized, yielding normally distributed data sets for down-stream comparison (right panel). These data suggested that the quantified proteomes spanned a similar concentration range. PASEF was able to quantify a higher number of proteins, which populated the lower domain of the measured concentration range.

These results indicated technological scalability to fewer cell populations. Based on the calculated LFQ abundance values, triplicate analysis of the same 10 ng proteome digest revealed low technical error (<1.9% RSD) and wide correlation (Pearson product moment correlation coefficient, $\rho \geq 0.85$). These performance metrics (Figure S1) were tested over a 4−5 log-order dynamic range and suit well to analyze endogenous biological concentrations. To gauge the scalability to smaller cell populations, the SCN proteome digest was measured in a dilution series. Considering an average ∼250 pg of proteome in a neuron,[32] Table 1 estimates protein identifications from approximately 40 cells to several cells and to subcellular amounts. Identification of 659 proteins from one to two cell-equivalent proteome amounts revealed improvement in sensitivity using TimsTOF PRO executing the PASEF data
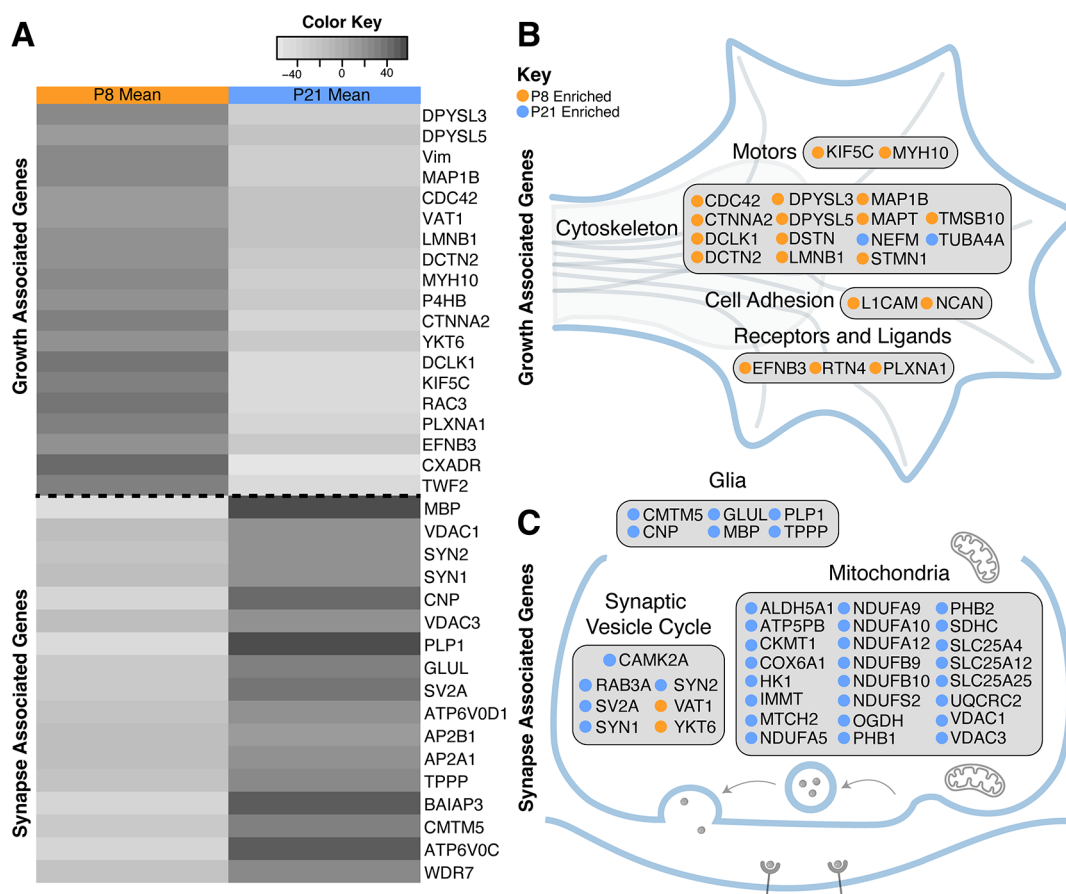
Figure 4. Pathway analysis uncovered key regulators of axon guidance and synaptogenesis associated with SCN maturation. (A) Gene set enrichment analysis revealed that growth-associated genes were enriched at P8, whereas synapse-associated genes were enriched at P21. Color key: white indicates relative protein depletion, and black indicates relative protein enrichment. (B, C) Modified Pathview schematics indicate proteins enriched in neurite growth and synaptic function at P8 and P21, respectively.

acquisition strategy. A list of the identified proteins is tabulated in Table 1 in the Supporting Information (Table S1).

Characterization of the Developing SCN Proteome. With enhanced sensitivity, we applied CE-ESI TimsTOF PRO MS to profile proteome changes in the developing SCN following eye-opening. A total of $n = 5$ independent biological replicate SCNs were characterized individually before eye-opening (P8), and four were measured after eye-opening (P21). A total of 1894 proteins were identified between the SCNs (Table S2). Each protein sample was assigned a unique identifier, although this information was intentionally hidden during data analysis and revealed only to facilitate the interpretation of the results at the end of the study.

We employed multivariate data analysis to survey systematic patterns in the proteome data set (Figure 3). The calculated LFQ intensities allowed us to approximate the concentration of each protein, serving as the basis for proteome-wide protein profiling. A total of 1066 proteins were quantified (Table S3). To identify age-dependent proteomic changes, we performed unsupervised principal component analysis (PCA) of the $\log_2$-normalized and median-centered quantitative proteome data. The first two principal components (PCs) explained ~31.7% and ~19.4% of variance in the data, respectively. Differential clustering of the samples in the calculated score plot (Figure 3A) revealed global differences between the tissue proteomes. Upon revealing the identities of the samples, these two groups corresponded to the P8 and P21 time points.

The PCA loading plot assessed the relative contribution of the various proteins to the observed systematic proteome differences. This analysis readily distinguished proteins with non-differential (900 total proteins) versus differential (166 total proteins) expression between P8 and P21 (Figure 3B). To investigate the global proteomic abundance similarities and differences during SCN maturation, we computed the pairwise Pearson correlation between all samples. The scores are hierarchically clustered (Figure 3C) and show significant correlations in protein expression between individual biological replicates of the same age and anticorrelated expression patterns between replicates of different ages (P8 vs P21).

We next confirmed the statistical significance of the observed proteome shifts. For each protein that was quantified in at least three biological replicates, the LFQ abundance was calculated, $\log_{10}$-transformed, mean-adjusted, and quantile normalized. Relative abundance changes in protein profiles were quantified using supervised DE analysis, to identify developmental enrichment at P8 vs P21 (Figure 3D). The computed fold changes and their statistical significance are listed in Table S4. At P8, we found 86 proteins significantly enriched, including many regulators of axon growth and guidance based on Gene Ontology (GO) annotation, consistent with the early postnatal time point (Figure 3D). At P21, 80 proteins were significantly enriched, including many with critical roles in synaptic maturation, neurotransmission, vesicle cycling, and mitochondrial function. The remaining 900 proteins, including many
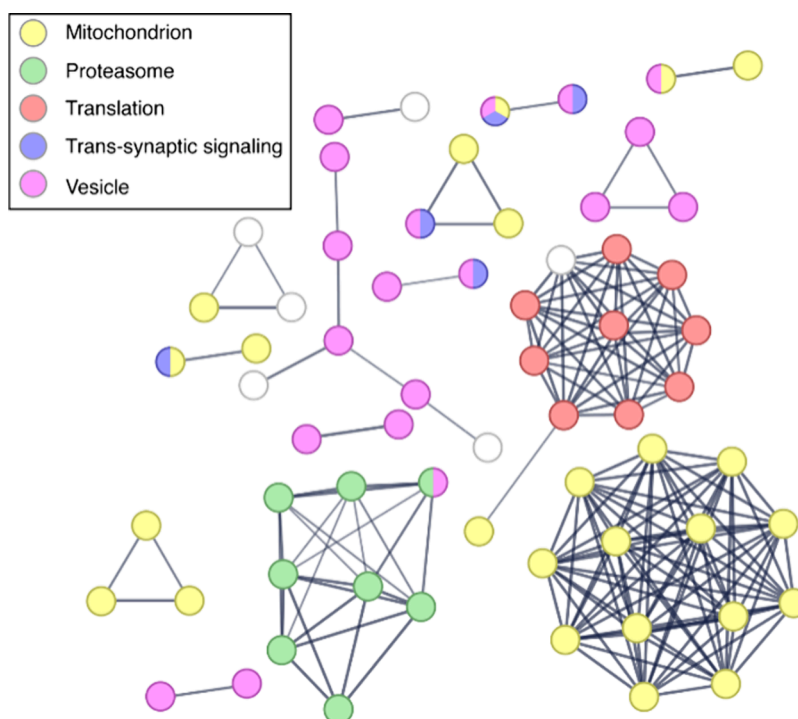
Figure 5. A STRINGdb network analysis of protein−protein interactions involving differentially expressed proteins. Nodes represent individual proteins identified in the differential expression analysis, which have at least one protein−protein interactor. Edges indicate that the proteins are part of a physical complex, and the edge weight indicates the strength of the database support.

housekeeping genes as well as some synaptic proteins (e.g., vesicular glutamate transporter 2, VGluT2), were not quantified as differentially expressed across development. A heatmap of the relative expression of the 166 differentially expressed proteins, ranked by fold change, for each sample revealed distinct clustering based on age, consistent with our PCA (Figure 3E).

Gene set enrichment analysis (GSEA) promised insights into developmentally regulated biological pathways (Figure 4A). Beginning with our list of proteins that were differentially expressed across the developmental time points, we used gProfiler[33] to identify protein enrichment within the GO database.[34] As shown in Table S5, this analysis identified the upregulation of growth-associated proteins found in GO categories for Growth Cone, Transport Along Microtubule, Regulation of Axonogenesis, and Regulation of Neuron Projection Development (Figure 4A). Additionally, we measured the upregulation of many synapse-associated proteins found in GO terms for Synaptic Vesicle Priming, Synaptic Vesicle Membrane, Synaptic Vesicle, and Presynapse (Figure 4A).

To complement our GSEA, we used Pathview[35] to visualize KEGG pathways[36] enriched in the identified differentially expressed proteins. At P8, we found significant enrichment of growth-associated proteins involved in axon guidance, consistent with postnatal innervation of the SCN by ipRGC axons in the mouse (Figure 4B).[37] This growth-associated group included key regulators of axon guidance and outgrowth including ephrin B3 and plexin A1, which are known regulators of midline crossing in the developing brain.[38−40] In contrast, we observed significant upregulation of synapse-associated proteins involved in synaptic function and the synaptic vesicle cycle at P21 (Figure 4C). Within this population were proteins associated with vesicle clustering, calcium sensing, vesicle filling, and vesicle fusion such as synapsins 1 and 2 (Syn 1 and 2). These

results are consistent with synaptic formation and maturation from P8 to P21 in the developing SCN.

To further characterize developmental changes in SCN protein networks, we investigated the known and predicted protein−protein interactions of the differentially expressed proteins using a STRINGdb[41] network model (Figure 5). From this database of protein−protein interactions, we identified protein subnetworks enriched with each differentially expressed species and its top 10 interacting proteins. The calculated network enrichment p value was 1.0×10^{-16}, indicating that the proteins in our DE results show significant (nonrandom) network interactions. Upon visual inspection, we identified clusters (putative protein−protein complexes) within the network that correlate with annotated GO terms including Proteasome, Translation, and Mitochondrion (Figure 5). Additionally, proteins within GO terms including Vesicle (pink) and Trans-synaptic Signaling (blue) were broadly distributed across the network (Figure 5). Together, these results highlight groups of proteins with related functions in proteostasis and energy production that are synchronously upregulated during SCN development between P8 and P21 (Figures 4 and 5 and Table S4).

Spatial Analysis by Super-Resolution Imaging. Having identified differentially regulated proteins in the developing SCN, we sought to provide spatial context to further interpret their biological significance. Based on our interest in the maturation of synaptic connections within the developing SCN, we focused on imaging synapsin 1 (Syn1) proteins. Syn1 plays a critical role in vesicle organization at presynaptic terminals,[42,43] and its expression was upregulated ∼3.2 fold from P8 to P21. This increase could reflect the growth of new synapses (increased presynaptic terminal number), synapse maturation (an increase in individual presynaptic terminal size), or additional trafficking of Syn1 protein within neurites. Differ-
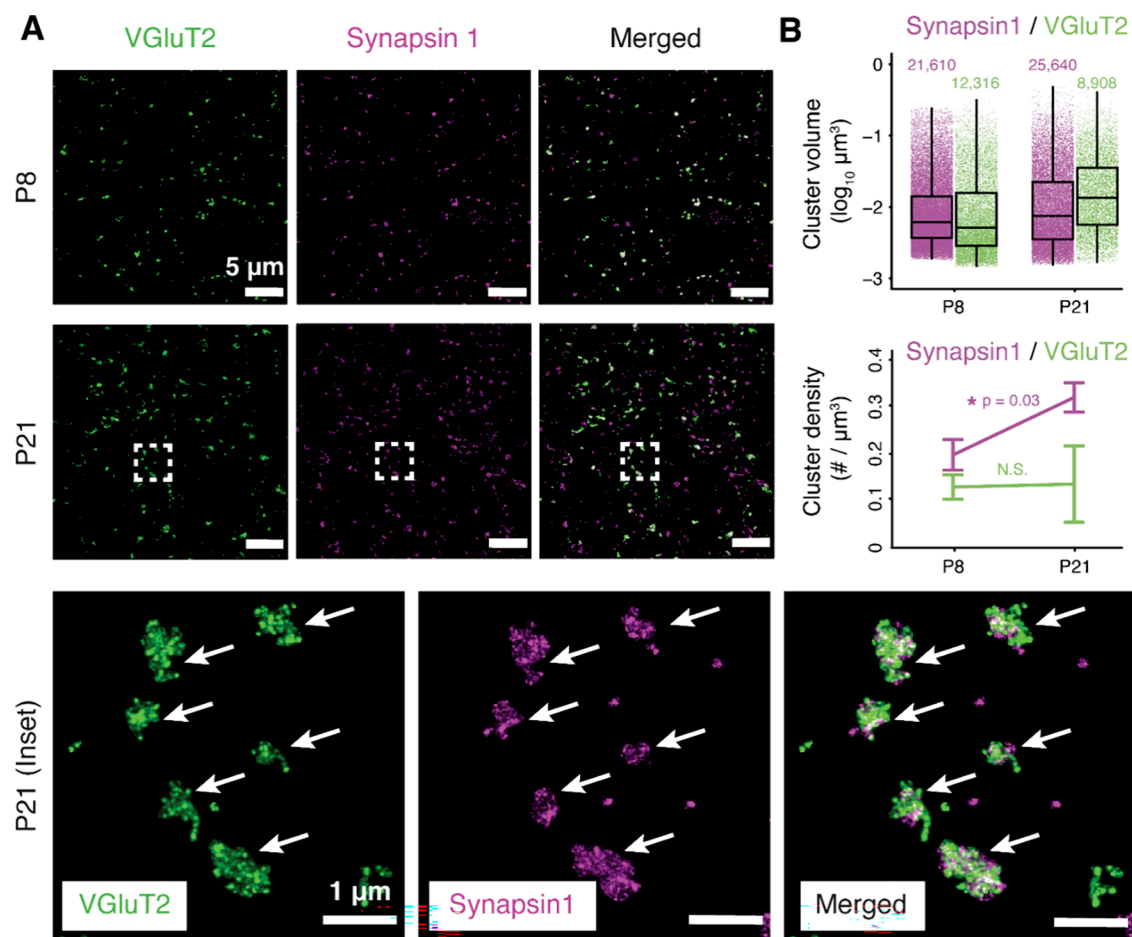
Figure 6. STORM imaging of SCN synaptic maturation before (P8) and after (P21) eye-opening. (A) Maximum projection image of VGluT2 (green) and Synapsin1 (magenta) at P8 (top) and P21 (middle panel). Insets (bottom panel) show colocalization of VGluT2 and Synapsin1 proteins at RHT synapses (arrows). (B) Quantitative image analysis. Top panel: cluster volumes of VGluT2 and Synapsin1 were not significantly different before and after eye-opening. Statistical analysis used a linear mixed model in which age was the fixed main factor, and technical replicate IDs were nested random factors. Jitter plots show all analyzed synaptic clusters (individual points) from two technical replicates at each age. The total cluster counts for each immunomarker at each age are shown above. Bottom panel: Synapsin1 cluster density increased significantly, while VGluT2 cluster density was stable over development. * $p < 0.05$, N.S. = not significant, Student's t test. Line plots reflect means ± S.E.M.s for two technical replicates. Scale bars: 5 μm in panels A (top/middle) and 1 μm in panel A (insets).

entiating between these possibilities is not possible using conventional fluorescence imaging tools, which lack the necessary spatial resolution to measure synaptic properties.[44] To address this challenge and provide a spatial interpretation for the MS results, we used a custom volumetric single-molecule localization super-resolution imaging approach based on STORM.[45] Using immunohistochemical labeling, we imaged Syn1 together with the vesicular glutamate transporter 2 (VGluT2) protein as a marker to identify retinohypothalamic (RHT) projections from ipRGCs to the SCN[46−49] (Figure 6). This dual-labeling strategy allowed us to investigate the relative maturation of retinal versus nonretinal synapses within the SCN while also corroborating our proteomic results, showing increased Syn1 expression and no change in VGluT2 expression over development.

The STORM images were quantitatively analyzed to identify presynaptic terminals (signal clusters) defined by connected image voxels (see SI). Following cluster identification, we measured the volume and signal intensity of each individual presynaptic terminal as well as the density of synapses within the total imaging volume. The mean cluster volume of individual Syn1- and VGluT2-expressing terminals did not change

significantly from P8 to P21 (Figure 6B, top panel; linear mixed model statistical analysis). In contrast, the density of Syn1-immunopositive terminals increased significantly from P8 to P21 ($p = 0.03$, Student's t test) while the density of VGluT2-expressing terminals was stable over the same period (Figure 6B, bottom panel). These results demonstrate a developmental increase in the total synapse number with no significant change in the average Syn1 or VGluT2 protein content of individual synapses (Figure 6B). The increase in the number of Syn1-immunopositive presynaptic terminals reveals ongoing synaptogenesis within non-RHT circuits (lacking presynaptic VGluT2 expression) between P8 and P21 in the developing SCN (Figure 6B).

■ CONCLUSIONS

This study systematically assessed CE-ESI on TimsTOF PRO MS to characterize the SCN proteome at two important developmental time points, before and after eye-opening; this work also demonstrates the complementary power of CE-MS proteomics and STORM imaging for addressing synaptic changes in the developing brain. Development of a micro-analytical CE-ESI timsTOF PASEF PRO MS technology

allowed us to characterize 1894 proteins between single SCNs by analyzing $<\sim$0.5% of the tissue proteome. This sensitivity estimates to $\sim$40 neurons, raising an opportunity for future studies to increasingly refine the physical resolution of proteomics in the brain. Quantitative profiling of 1066 of these proteins revealed systematic reorganization of the developing SCN proteome, with significant developmental changes detected for 166 proteins, many with known and important biological functions in mitochondrial function, proteostasis, axon guidance, synapse function, and glial cell maturation.

Guided by microanalytical proteomics, super-resolution spatial imaging helped to interpret the biological relevance of proteome changes in the developing SCN with previously unavailable insights. Specifically, we found that Syn1-immuno-positive synaptic connections continue to form following eye-opening, with $\sim$65% increase in density from P8 to P21. At the same time, the average presynaptic vesicle pool size of individual Syn1-expressing terminals remains stable. By immunostaining for VGluT2, we found that RHT input to the SCN showed a smaller overall increase in density ($<$5%) from P8 to P21. This result is consistent with previous electron microscopy measurements, showing that RHT synapse density is adult-like prior to eye-opening in the rat.[50] Interestingly, the mean volumes of both VGluT2- and Syn1-immunopositive terminals in the SCN were comparable before and after eye-opening. Together, these results suggest that SCN circuit maturation after eye-opening occurs by synapse addition without a significant change in presynaptic size or protein abundance within individual synaptic terminals. This pattern of RHT development stands in contrast to the development of image-forming retinal projections to the dorsal lateral geniculate nucleus (dLGN), which show a progressive increase in synapse size over development before and after eye-opening.[51−53]

The microanalytical platform developed here integrated CE-ESI with TimsTOF PRO MS to demonstrate the identification of $>$1800 different proteins. The analyses permitted proteome quantification with high accuracy, precision, and reproducibility (μ = 1.9% RSD, Pearson $\rho > 0.85$), without needing functional probes such as antibodies. The results from such discovery MS measurements provide throughput and convenience. Super-resolution imaging by STORM complements MS micro-proteomics by measuring the spatial organization of targeted proteins, thus helping to generate and test hypotheses. In the future, we envision that the combination of microanalytical CE-ESI TimsTOF PRO MS, super-resolution microscopy, and advanced genetic labeling strategies will enable new experiments investigating the subcellular molecular organization and development of targeted microcircuits in the brain.[54]

ASSOCIATED CONTENT

Supporting Information

The Supporting Information is available free of charge at https://pubs.acs.org/doi/10.1021/acs.analchem.3c01987.

Supplementary methods, protocols, and approaches (PDF)

Protein identification and quantification and GO analysis (XLSX)

AUTHOR INFORMATION

Corresponding Authors

Colenso M. Speer − *Department of Biology, University of Maryland, College Park, Maryland 20742, United States*; Phone: (1) 301-405-0178; Email: cspeer@umd.edu

Peter Nemes − *Department of Chemistry and Biochemistry, University of Maryland, College Park, Maryland 20742, United States;* orcid.org/0000-0002-4704-4997; Phone: (1) 301-405-0373; Email: nemes@umd.edu; Fax: (1) 301-314-9121

Authors

Sam B. Choi − *Department of Chemistry and Biochemistry, University of Maryland, College Park, Maryland 20742, United States*

Tarlan Vatan − *Department of Biology, University of Maryland, College Park, Maryland 20742, United States*

Theresa A. Alexander − *Department of Biology, University of Maryland, College Park, Maryland 20742, United States*

Chenghang Zhang − *Department of Biology, University of Maryland, College Park, Maryland 20742, United States*

Shyrice M. Mitchell − *Department of Biology, University of Maryland, College Park, Maryland 20742, United States*

Complete contact information is available at:
https://pubs.acs.org/10.1021/acs.analchem.3c01987

Author Contributions

#S.B.C., T.V., and T.A.A. contributed equally to this study.

Author Contributions

C.M.S. and P.N. designed the study. P.N. designed the MS proteomics experiments. T.V. and C.M.S. designed the STORM imaging experiments. S.M.M. isolated the tissues for proteomic analysis. S.B.C. and P.N. developed the MS technology. S.B.C processed the tissues and measured their proteomes. T.A.A. and S.B.C. performed chemometrics. T.A.A. performed all bio-informatic analyses. T.V. performed STORM sample prepara-tion and imaging. C.Z. and T.V. analyzed STORM imaging data. S.B.C., T.V., T.A.A., C.M.S., and P.N. interpreted the results. S.B.C., T.V., T.A.A., C.M.S., and P.N. prepared the manuscript. All coauthors commented on the final manuscript.

Notes

The authors declare no competing financial interest.

REFERENCES

(1) Lazzerini Ospri, L.; Prusky, G.; Hattar, S. *Annu. Rev. Neurosci.* **2017**, *40*, 539−556.

(2) Fernandez, D. C.; Fogerson, P. M.; Lazzerini Ospri, L.; Thomsen, M. B.; Layne, R. M.; Severin, D.; Zhan, J.; Singer, J. H.; Kirkwood, A.; Zhao, H.; Berson, D. M.; Hattar, S. *Cell* **2018**, *175* (1), 71−84.

(3) Do, M. T. H. *Neuron* **2019**, *104*, 205−226.

(4) Hastings, M. H.; Maywood, E. S.; Brancaccio, M. *Nat. Rev. Neurosci.* **2018**, *19*, 453−469.

(5) Hatcher, N. G.; Atkins, N., Jr.; Annangudi, S. P.; Forbes, A. J.; Kelleher, N. L.; Gillette, M. U.; Sweedler, J. V. *Proc. Natl. Acad. Sci.* **2008**, *105*, 12527−12532.

(6) Lee, J. E.; Atkins, N.; Hatcher, N. G.; Zamdborg, L.; Gillette, M. U.; Sweedler, J. V.; Kelleher, N. L. *Mol. Cell. Proteomics* **2010**, *9*, 285−297.

(7) Mendoza-Viveros, L.; Chiang, C. K.; Ong, J. L. K.; Hegazi, S.; Cheng, A. H.; Bouchard-Cannon, P.; Fana, M.; Lowden, C.; Zhang, P.; Bothorel, B.; Michniewicz, M. G.; Magill, S. T.; Holmes, M. M.; Goodman, R. H.; Simonneaux, V.; Figeys, D.; Cheng, H. Y. M. *Cell Rep.* **2017**, *19*, 505−520.

(8) Deery, M. J.; Maywood, E. S.; Chesham, J. E.; Sládek, M.; Karp, N. A.; Green, E. W.; Charles, P. D.; Reddy, A. B.; Kyriacou, C. P.; Lilley, K. S.; Hastings, M. H. *Curr. Biol.* **2009**, *19*, 2031−2036.

(9) Lee, J. E.; Zamdborg, L.; Southey, B. R.; Atkins, N.; Mitchell, J. W.; Li, M.; Gillette, M. U.; Kelleher, N. L.; Sweedler, J. V. *J. Proteome Res.* **2013**, *12*, 585−593.

(10) Tian, R.; Alvarez-Saavedra, M.; Cheng, H. Y. M.; Figeys, D. *Mol. Cell. Proteomics* **2011**, *10*, M110.007252.

(11) Chiang, C. K.; Mehta, N.; Patel, A.; Zhang, P.; Ning, Z.; Mayne, J.; Sun, W. Y. L.; Cheng, H. Y. M.; Figeys, D.; Kramer, A. *PLoS Genet.* **2014**, *10*, No. e1004695.

(12) Hebert, A. S.; Richards, A. L.; Bailey, D. J.; Ulbrich, A.; Coughlin, E. E.; Westphall, M. S.; Coon, J. J. *Mol. Cell Proteomics* **2014**, *13*, 339−347.

(13) Picotti, P.; Clement-Ziza, M.; Lam, H.; Campbell, D. S.; Schmidt, A.; Deutsch, E. W.; Rost, H.; Sun, Z.; Rinner, O.; Reiter, L.; Shen, Q.; Michaelson, J. J.; Frei, A.; Alberti, S.; Kusebauch, U.; Wollscheid, B.; Moritz, R. L.; Beyer, A.; Aebersold, R. *Nature* **2013**, *494*, 266−270.

(14) Sun, L.; Dubiak, K. M.; Peuchen, E. H.; Zhang, Z.; Zhu, G.; Huber, P. W.; Dovichi, N. J. *Anal. Chem.* **2016**, *88*, 6653−6657.

(15) Saha-Shah, A.; Esmaeili, M.; Sidoli, S.; Hwang, H.; Yang, J.; Klein, P. S.; Garcia, B. A. *Anal. Chem.* **2019**, *91*, 8891−8899.

(16) Woo, J.; Williams, S. M.; Markillie, L. M.; Feng, S.; Tsai, C.-F.; Aguilera-Vazquez, V.; Sontag, R. L.; Moore, R. J.; Hu, D.; Mehta, H. S.; Cantlon-Bruce, J.; Liu, T.; Adkins, J. N.; Smith, R. D.; Clair, G. C.; Pasa-Tolic, L.; Zhu, Y. *Nat. Commun.* **2021**, *12*, 6246.

(17) Petelski, A. A.; Emmott, E.; Leduc, A.; Huffman, R. G.; Specht, H.; Perlman, D. H.; Slavov, N. *Nat. Protoc.* **2021**, *16*, 5398−5425.

(18) Meier, F.; Brunner, A. D.; Koch, S.; Koch, H.; Lubeck, M.; Krause, M.; Goedecke, N.; Decker, J.; Kosinski, T.; Park, M. A.; Bache, N.; Hoerning, O.; Cox, J.; Rather, O.; Mann, M. *Mol. Cell. Proteomics* **2018**, *17*, 2534−2545.

(19) Brunner, A.; Thielert, M.; Vasilopoulou, C.; Ammar, C.; Coscia, F.; Mund, A.; Hoerning, O. B.; Bache, N.; Apalategui, A.; Lubeck, M.; Richter, S.; Fischer, D. S.; Raether, O.; Park, M. A.; Meier, F.; Theis, F. J.; Mann, M. *Mol. Syst. Biol.* **2022**, *18*, No. e10798.

(20) Johnson, K. R.; Gregus, M.; Kostas, J. C.; Ivanov, A. R. *Anal. Chem.* **2022**, *94*, 704−713.

(21) Shen, B.; Pade, L. R.; Choi, S. B.; Muñoz-LLancao, P.; Manzini, M. C.; Nemes, P. *Front. Chem.* **2022**, *10*, No. 863979.

(22) Choi, S. B.; Polter, A. M.; Nemes, P. *Anal. Chem.* **2022**, *94*, 1637−1644.

(23) Lombard-Banek, C.; Li, J.; Portero, E. P.; Onjiko, R. M.; Singer, C. D.; Plotnick, D. O.; Al Shabeeb, R. Q.; Nemes, P. *Angew. Chem.* **2021**, *60*, 12852−12858.

(24) Lombard-Banek, C.; Moody, S. A.; Manzini, M. C.; Nemes, P. *Anal. Chem.* **2019**, *91*, 4797−4805.

(25) Choi, S. B.; Muñoz-LLancao, P.; Manzini, M. C.; Nemes, P. *Anal. Chem.* **2021**, *93*, 15964−15972.

(26) Sun, L.; Zhu, G.; Zhao, Y.; Yan, X.; Mou, S.; Dovichi, N. J. *Angew. Chem., Int. Ed.* **2013**, *52*, 13661−13664.

(27) Sun, L.; Zhu, G.; Zhang, Z.; Mou, S.; Dovichi, N. J. *J. Proteome Res.* **2015**, *14*, 2312−2321.

(28) Johnson, K. R.; Gao, Y.; Greguš, M.; Ivanov, A. R. *Anal. Chem.* **2022**, *94*, 14358−14367.

(29) Perez-Riverol, Y.; Bai, J.; Bandla, C.; García-Seisdedos, D.; Hewapathirana, S.; Kamatchinathan, S.; Kundu, D. J.; Prakash, A.; Frericks-Zipper, A.; Eisenacher, M.; Walzer, M.; Wang, S.; Brazma, A.; Vizcaíno, J. A. *Nucleic Acids Res.* **2022**, *50*, D543−D552.

(30) DeLaney, K.; Jia, D.; Iyer, L.; Yu, Z.; Choi, S. B.; Marvar, P. J.; Nemes, P. *Anal. Chem.* **2022**, *94*, 9018−9025.

(31) Lombard-Banek, C.; Reddy, S.; Moody, S. A.; Nemes, P. *Mol. Cell. Proteomics* **2016**, *15*, 2756−2768.

(32) Choi, S. B.; Zamarbide, M.; Manzini, M. C.; Nemes, P. *J. Am. Soc. Mass Spectrom.* **2017**, *28*, 597−607.

(33) Kolberg, L.; Raudvere, U.; Kuzmin, I.; Vilo, J.; Peterson, H.; Kolberg, L.; Raudvere, U.; Kuzmin, I.; Vilo, J.; Peterson, H. *F1000Research* **2020**, *9*, 709.

(34) Ashburner, M.; Ball, C. A.; Blake, J. A.; Botstein, D.; Butler, H.; Cherry, J. M.; Davis, A. P.; Dolinski, K.; Dwight, S. S.; Eppig, J. T.; Harris, M. A.; Hill, D. P.; Issel-Tarver, L.; Kasarskis, A.; Lewis, S.; Matese, J. C.; Richardson, J. E.; Ringwald, M.; Rubin, G. M.; Sherlock, G. *Nat. Genet.* **2000**, *25*, 25−29.

(35) Luo, W.; Brouwer, C. *Bioinformatics* **2013**, *29*, 1830−1831.

(36) Kanehisa, M. *Nucleic Acids Res.* **2000**, *28*, 27−30.

(37) McNeill, D. S.; Sheely, C. J.; Ecker, J. L.; Badea, T. C.; Morhardt, D.; Guido, W.; Hattar, S. *Neural Dev.* **2011**, *6*, 1−10.

(38) Kuwajima, T.; Yoshida, Y.; Takegahara, N.; Petros, T. J.; Kumanogoh, A.; Jessell, T. M.; Sakurai, T.; Mason, C. *Neuron* **2012**, *74*, 676−690.

(39) Bergemann, A. D.; Zhang, L.; Chiang, M. K.; Brambilla, R.; Klein, R.; Flanagan, J. G. *Oncogene* **1998**, *16*, 471−480.

(40) Yokoyama, N.; Romero, M. I.; Cowan, C. A.; Galvan, P.; Helmbacher, F.; Charnay, P.; Parada, L. F.; Henkemeyer, M. *Neuron* **2001**, *29*, 85−97.

(41) Szklarczyk, D.; Gable, A. L.; Nastou, K. C.; Lyon, D.; Kirsch, R.; Pyysalo, S.; Doncheva, N. T.; Legeay, M.; Fang, T.; Bork, P.; Jensen, L. J.; von Mering, C. *Nucleic Acids Res.* **2021**, *49*, D605−D612.

(42) Pieribone, V. A.; Shupliakov, O.; Brodin, L.; Hilfiker-Rothenfluh, S.; Czernik, A. J.; Greengard, P. *Nature* **1995**, *375*, 493−497.

(43) Milovanovic, D.; Wu, Y.; Bian, X.; De Camilli, P. *Science* **2018**, *361*, 604−607.

(44) Sigal, Y. M.; Speer, C. M.; Babcock, H. P.; Zhuang, X. *Cell* **2023**, *163*, 493−505.

(45) Vatan, T.; Minehart, J. A.; Zhang, C.; Agarwal, V.; Yang, J.; Speer, C. M. *STAR Protoc.* **2021**, *2*, No. 100971.

(46) El-Danaf, R. N.; Krahe, T. E.; Dilger, E. K.; Bickford, M. E.; Fox, M. A.; Guido, W. *Neural Dev.* **2015**, *10*, 1−17.

(47) Fujiyama, F.; Hioki, H.; Tomioka, R.; Taki, K.; Tamamaki, N.; Nomura, S.; Okamoto, K.; Kaneko, T. *J. Comp. Neurol.* **2003**, *465*, 234−249.

(48) Hammer, S.; Carrillo, G. L.; Govindaiah, G.; Monavarfeshani, A.; Bircher, J. S.; Su, J.; Guido, W.; Fox, M. A. *Neural Dev.* **2014**, *9*, 1−21.

(49) Land, P. W.; Kyonka, E.; Shamalla-Hannah, L. *Brain Res.* **2004**, *996*, 251−254.

(50) Moore, R. Y.; Bernstein, M. E. *J. Neurosci.* **1989**, *9*, 2151−2162.

(51) Bickford, M. E.; Slusarczyk, A.; Dilger, E. K.; Krahe, T. E.; Kucuk, C.; Guido, W. *J. Comp. Neurol.* **2010**, *518*, 622−635.

(52) Monavarfeshani, A.; Stanton, G.; Van Name, J.; Su, K.; Mills, W. A.; Swilling, K.; Kerr, A.; Huebschman, N. A.; Su, J.; Fox, M. A. *eLife* **2018**, *7*, No. e33498.

(53) Zhang, C.; Yadav, S.; Speer, C. M. *Cell Rep.* **2023**, *42*, No. 112085.

(54) Minehart, J. A.; Speer, C. M. *Front. Synaptic Neurosci.* **2020**, *12*, No. 615059.